Tiny Clusters for Big Impact in T Cell Activation

Guillaume Le Saux[1,2,†], Piotr Nowakowski[3,†], Esti Toledo[1,2], Sivan Tzdaka[1,2], Shagufta Naaz[1,2], Yuval Segal[1,2], Brit Maman[1,2], Jatin Jawhir Pandit[1,2], Muhammed Iraqi[4], Abed Al-Kader Yassin[4], Angel Porgador[4], Ana-Sunčana Smith[3,5,‡] and Mark Schvartzman[1,2,‡]

[1]*Department of Materials Engineering, Faculty of Engineering, Ben-Gurion University of the Negev, , Beer-Sheva 84105, Israel*
[2]*Ilse Katz Institute for Nanoscale Science and Technology, Ben-Gurion University of the Negev Beer-Sheva 84105, Israel*
[3]*Group for Computational Life Sciences, Division of Physical Chemistry, Ruđer Bošković Institute, Bijenička 54, 10000, Zagreb, Croatia*
[4]*Department of Microbiology and immunology, and Genetics, Faculty of Health Sciences, Ben-Gurion University of the Negev, , Beer-Sheva 84105, Israel*
[5]*PULS Group, Institut für Theoretische Physik, IZNF, Friedrich-Alexander-Universität Erlangen-Nürnberg, Cauerstraße 3, 91058 Erlangen, Germany*

E-mail: smith@physik.fau.de, asmith@irb.hr; marksc@bgu.ac.il

[†] Equally contributing authors

[‡]Corresponding authors

The regulation of T cell activation via engineered arrays holds significant biomedical potential. While average antibody density is known to influence T cell activation, antibody clustering has shown limited benefits. This study challenges this perspective through combined experimental and theoretical approaches. By employing nanolithographically patterned arrays, we show that full T cell activation is achievable with a small number of densely packed antibody clusters—even at average densities where homogeneous or sparsely clustered distributions are insufficient for full activation. These results align with the membrane-fluctuation model that considers cooperative bonding and mechanical feedback. Our findings highlight the importance of the spatial organization of activating ligands and provide a framework for designing improved T cell activation platforms for immunotherapy.

T cell activation, Antibody Clustering, Nanolithography, Membrane Fluctuation Model

T cells—key players in adaptive immunity, recognize pathogens by binding antigens on cell surfaces via T cell receptors (TCRs). Activation of T cells requires two signals: TCR binding to antigen-MHC complexes on antigen-presenting cells (APCs) and costimulatory binding of CD28 receptor to ligands like B7-1. This triggers a signaling cascade leading to T cell activation, proliferation, differentiation into effector T cells and generation of memory T cells. Understanding T cell activation is crucial not only for the fundamental understanding of T cell immunity but also for advancing new immunotherapies. For example, the generation of chimeric antigen receptor (CAR) T cells[1] requires *ex vivo* T cell activation, which significantly affects the efficiency of CAR transduction and the proliferation of engineered T cells.[2–4]

Ex vivo, T cells are typically activated by stimulating TCR/CD3 and CD28 with antibodies, either in soluble form or bound to artificial antigen-presenting surfaces like plastic microbeads. While both ligand–receptor and antibody–receptor interactions trigger the same signaling pathways, key differences remain; notably, the lower affinity and fast kinetics of ligand–receptor binding enable serial triggering, where one ligand can activate multiple TCRs.[5] High-affinity antibody–receptor binding prevents serial triggering, leading to distinct spatial requirements for T cell activation compared to ligands[6]. Proposed mechanisms of T cell activation are based on: (i) TCR conformation change upon ligand binding,[7] (ii) kinetic segregation,[8,9] where exclusion of large inhibitory phosphatases from tight receptor-ligand region shifts the kinase–phosphatase balance, and (iii) TCR clustering that increases the concentration of signaling molecules.[10,11] These clusters may grow from a few hundred nanometer size in early stages[12,13] to few microns in mature T cell contacts with the target cell.[14–16] The clustering, even at very low ligand concentrations,[17] is promoted by the mobility of ligands and receptors within the cell membrane, optimizing activation.[18] Even so, *ex vivo* activation platforms, like antibody-coated microbeads—the standard in T cell production—use static antibodies, fixing the position of bonded receptors.[19–22] Besides the simplicity of production, the preference for *ex-vivo* T cell activation platforms with a homogeneous distribution of antibodies stems from the lack of consensus on the role of molecular clustering in T cell activation (reviewed in Ref. [24]).

The pre-existence of nanoscale clusters of TCR in resting T cells, however, remains controversial[23] and the mechanism and role of clustering is still highly debated.[24,25] So far, self-assembled continuous arrays of ligands or antibodies were used to demonstrate the importance of their distribution for activation.[26,27] However, these arrays could not differentiate between the effects of overall density and clustering. Arrays with independently varied clustering and density revealed spatial control of receptor binding but found no impact of TCR clustering on T cell spreading.[23] Importantly, these studies did not assess the effects of antibody/ligand clustering per-se on T cell response, and focused on activating signaling, neglecting the costimulatory CD28 signaling.

In this work, we focus on understanding the consequences of joint presentation of anti-CD3 and anti-CD28 antibodies in T cell activation, and on resolving the effects of surface density and clustering of these antibodies. We first correlate T cell activation and cytotoxic function with the global density of the two

homogeneously distributed proteins and determine the threshold homogeneous density at which T cell activation cannot be determined. Fixed at this global density, we then engineer arrays with antibodies grouped into dense and sparse clusters of varying sizes. This allows us to unambiguously identify the compensatory effects of clustering. Surprisingly, we find that for the same low global density of antibodies, tightly packed small clusters induce full T cell activation, while either homogeneously distributed antibodies or antibodies grouped into differently sized diluted clusters have no effect (Fig. 1). These findings are explained by the Membrane Fluctuation Model (MFM) which links antibody–receptor recognition to cellular activity.[28] Our results highlight the critical role of nanoscale antibody clustering in regulating T cell responses, offering insights into immunity and biomaterial design for immunomodulation.

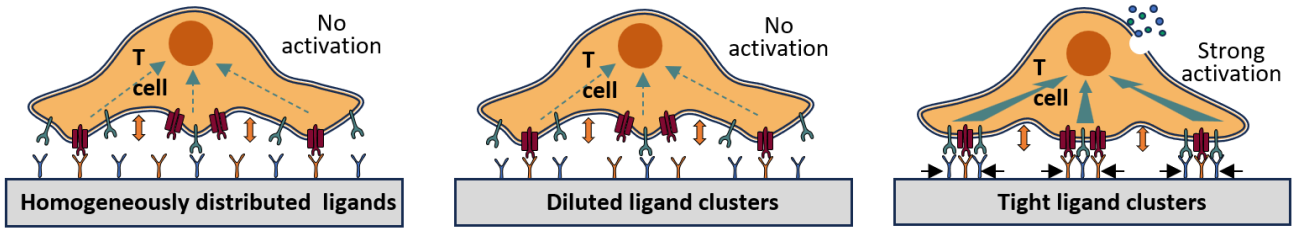

.

Figure 1. Schematic plot of T cell binding to the substrate with controlled distribution of antibodies. Cell activation is not achieved when antibodies are homogeneously distributed (left panel) or grouped into diluted clusters (middle panel) over the surface at low global densities. As presented on the right panel, full T cell activation is achieved by binding to the substrate with the density of antibodies that is the same as on left panel, but now antibodies are clustered in very dense small clusters

To establish a baseline for studying the effects of antibody density and clustering on T cell activation, we first examined the T cell activation by surfaces coated with homogeneously distributed α-CD3/α and CD28 at a ratio of 1:1. The surfaces were produced by functionalizing silicon with (3-Aminopropyl)tiethoxysilane (APTES), followed by the attachment of polyethylene glycol (PEG)-carboxylic acid terminated with biotin, to which biotinylated antibody mixtures with different dilutions were attached through a neutravidin bridge. Three types of surfaces were used: surfaces with 100% antibody coverage, and surfaces with α-CD3/α-CD28 diluted with human immunoglobulin G2 (IgG2a) at 1:10 and 1:100 ratios. By considering discoid antibody footprint of 5 nm diameter and densely packed antibody arrangement,[29] we estimate that this produced global α-CD3 and α-CD28 densities of ~400, ~4000, and ~40 000 antibodies/μm² (Fig. 2 a,b).

Peripheral Blood Mononuclear Cells (PBMCs) from a healthy donor were used as a source of T cells. The PBMCs were seeded onto patterned surfaces in 96-well plates, stimulated, and then stained for CD3, CD4, CD8, for flow cytometry analysis. The activation was assessed by flow cytometry using two markers: CD69 after 18 hours of stimulation, and CD107a (degranulation marker) after 4 hours of stimulation. As expected, the lowest α-CD3 and α-CD28 density produced only ~40% CD69-positive cells, compared to ~80% for

surfaces at full α-CD3 and α-CD28 coverage. CD107a expression in CD8+ cells was only ~2% at the lowest density versus ~25% at the highest, with negligible degranulation in CD4+ T cells due to their non-cytotoxic nature. This suggests that our lowest homogeneous density is insufficient to fully activate T cells. However, the activation gradually increases with density until fully activated cells are observed at surfaces continuously covered by antibodies, consistently with activation observed using only α-CD3.[20] Also, similar trend of activation vs. antibody density was observed using IFN-γ assessed by ELISA after 18 hrs. of activation, although with less pronounced differences between various densities, likely to the contributions of other cells presenting in PBMCs (Fig. S1).

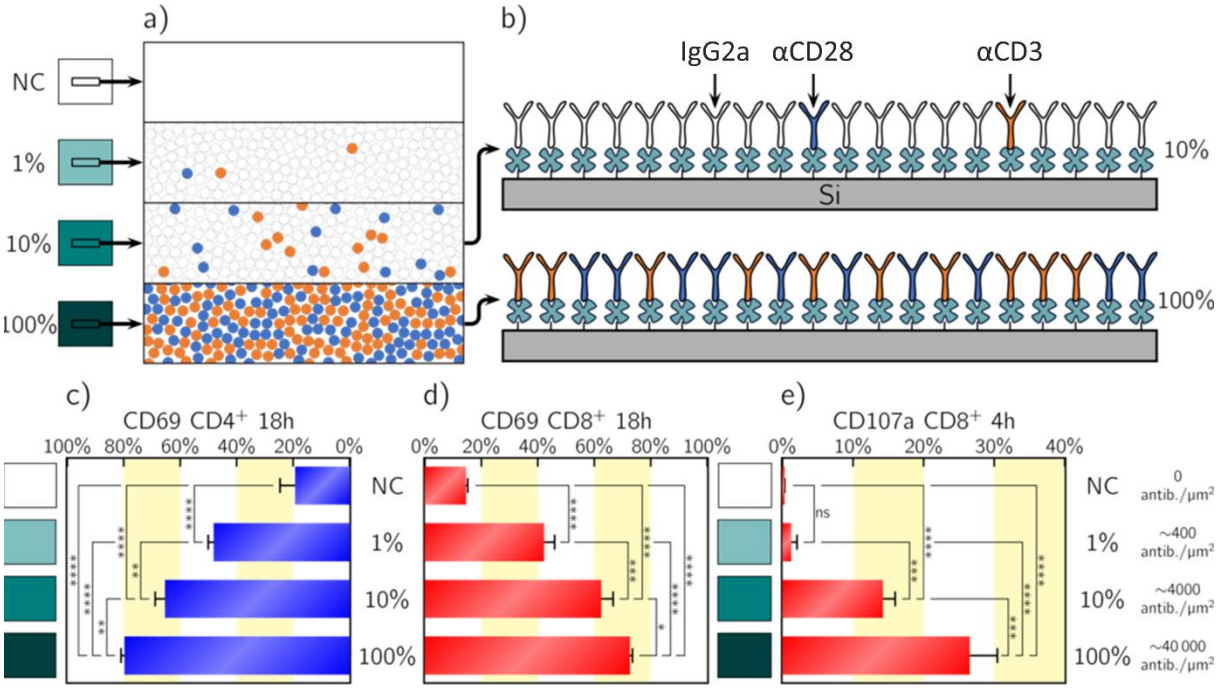

Figure 2. a) Schematic plot of surface covered with continuous array of antibodies. For 100% continuous array, the surface is fully covered with α-CD3 and α-CD28 antibodies (schematically denoted as orange and blue dots, respectively). For 10% continuous array, only 10% of antibodies are α-CD3/α-CD28. The remaining antibodies are IgG2a isotype controls, which do not bind T cells, schematically denoted with white circles. For 1% continuous array, only 1% of antibodies bind to T cell. Finally, for negative control (NC) there are no antibodies on the substrate. b) Schematic illustration of the surface covered with antibodies for 10% and 100% continuous arrays. c) Experimentally measured quantification of CD69 expression for $CD4^+$ cells stimulated on negative control (NC) and continuous arrays (1%, 10%, and 100%) with various dilutions of binding antibodies. d) Experimentally measured quantification of CD69 expression for $CD8^+$ cells stimulated on negative control and continuous arrays. e) Experimentally measured quantification of CD107a expression for $CD8^+$ cells stimulated on negative control and continuous arrays.

Following this initial observation, we selected the 1:100 (α-CD3/α-CD28):IgG2a dilution as a benchmark for full T cell activation, to examine the potentially compensatory effect of antibody clustering.

To that end, we designed a series of arrays of disk-shaped antibody clusters, maintaining the 1:100 (α-CD3/α-CD28):IgG2a dilution within each disk. Disk sizes ranged from 100 nm to 1 μm, with center-to-center spacing set at twice the disks diameter (Fig. 3a, patterns A–D). In all these configurations, despite different sizes and separations, disks, and therefore the antibody clusters occupied approximately 23% of the total surface area, resulting in a theoretical global α-CD3/α-CD28 density of ~90 antibodies/μm².

These arrays (A–D) were created using nanosphere lithography, an ideal method for producing dense nanoscale patterns.[30] Polystyrene nanospheres were assembled into a closely packed hexagonal monolayer on a silicon surface, using either the Langmuir–Blodgett method for 200 nm spheres or a dry method for larger spheres.[31] The spheres were etched by oxygen plasma to halve their diameter, followed by gold evaporation in the interstices of the nanosphere array Nanosphere lift-off created a hexagonal array of silicon discs surrounded by a gold background (Fig. S2). This results in a set of patterns which we denominate with three indices [disk diameter in nm / disk periodicity in nm / percentage of α-CD3/α-CD28 in the antibody mix within the disk]. As shown in Fig. 3a, pattern A, noted [100/200/1] yields 29 disks /μm^2, pattern B [250/500/1] 4.6 disks/μm^2, pattern C [500/1000/1] 1.2 disks/μm^2, and pattern D [1000/2000/1] 0.29 disk/μm^2. These designs allow us to assess if the introduction of a particular length scale in the antibody organization affects T cell activation.

Also, to investigate the role of local antibody density within clusters, we designed a pattern of disks as small as in pattern A (100 nm) but separated by 2 μm (Fig. 3a, pattern E, and Fig. S3). In these 100 nm disks, the antibodies were not diluted, i.e. contained 100% α-CD3/α-CD28, and thus mimicked the dimensions of receptor clusters in resting T cells.[25] For pattern E [100/2000/100], the 10-fold larger distance between the clusters was designed to keep the global density of ~90 antibodies/μm² as in patterns A–D. This pattern, denominated as pattern E [100/2000/100] with 0.29 disks /μm^2, was produced by electron-beam lithography of negative tone resist, which was followed by gold evaporation and liftoff. Notably, a T cell with a typical spreading area of 5–10 μm^2 can be exposed only to one or two such clusters on average.

Finally, along the same line of thought that the density of proteins within clusters and not the cluster size itself or the number of clusters affects activation, we prepared a pattern with a geometry identical to that of cluster A, but increased the concentration of α-CD3/α-CD28 to 10% by 1:10 (α-CD3/α-CD28):IgG2a dilution (pattern F [100/200/10], achieving an average density of ~900 antibodies/μm^2 and 29 disks/μm^2). All patterns, regardless of their fabrication methods, were functionalized by various mixtures of α-CD3/α-CD28 and IgG2a, which were linked to oxidized silicon nanodiscs *via* APTES, PEG, and biotin chemistries. The surrounding gold was passivated by PEG to prevent non-specific binding. Biofunctionalization specificity was confirmed by confocal microscopy (Fig. 3 c,d).

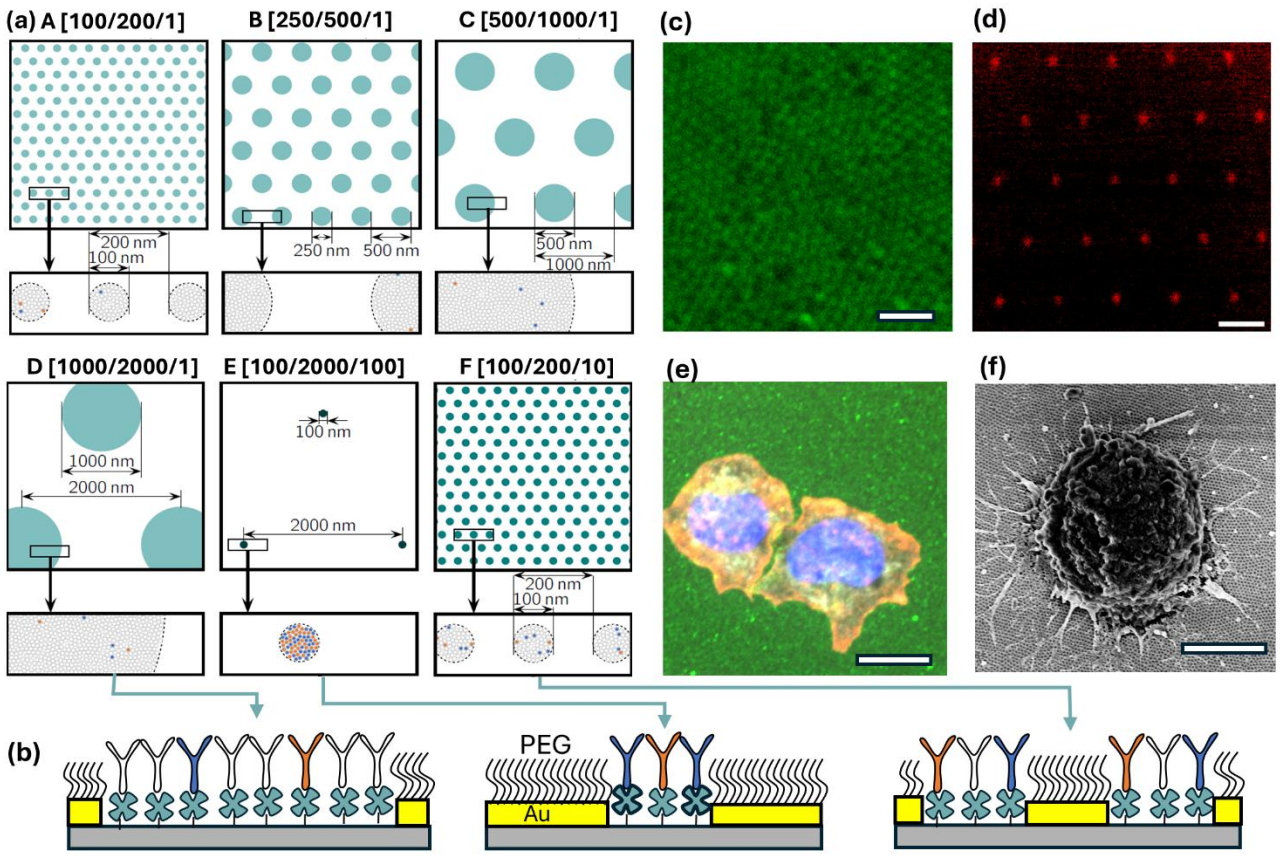

Figure 3. a) Schematic plots of the patterns used in our study. Each pattern is described with three numbers: [distance between neighboring clusters in nm/diameter of each cluster in nm/dilution of the antibodies in percentages]. Patterns A, B, C, D, and E have the same overall density of antibodies ~90 μm^{-2}. Pattern F has a density of ~900 μm^{-2}. b) Schematic plots of the patterned substrates with attached antibodies. c) High resolution image of clusters of antibodies visualized through the green fluorescently-tagged neutravidin. Scale bar : 1 µm. d) Fluorescent image of 100 nm antibody clusters separated by 2 µm. Scale bar : 2 µm. e) Fluorescent microscopy of T cells spread on an array of antibody clusters. Avidin used for binding the antibodies to silicon surfaces was tagged with green, and the cells were tagged with red phalloidin for cytoskeleton and blue DAPI for nucleus. Scale bar: 5 µm f) Scanning electron micrograph of T cell spread on the nanoarray. Scale bar: 5 µm

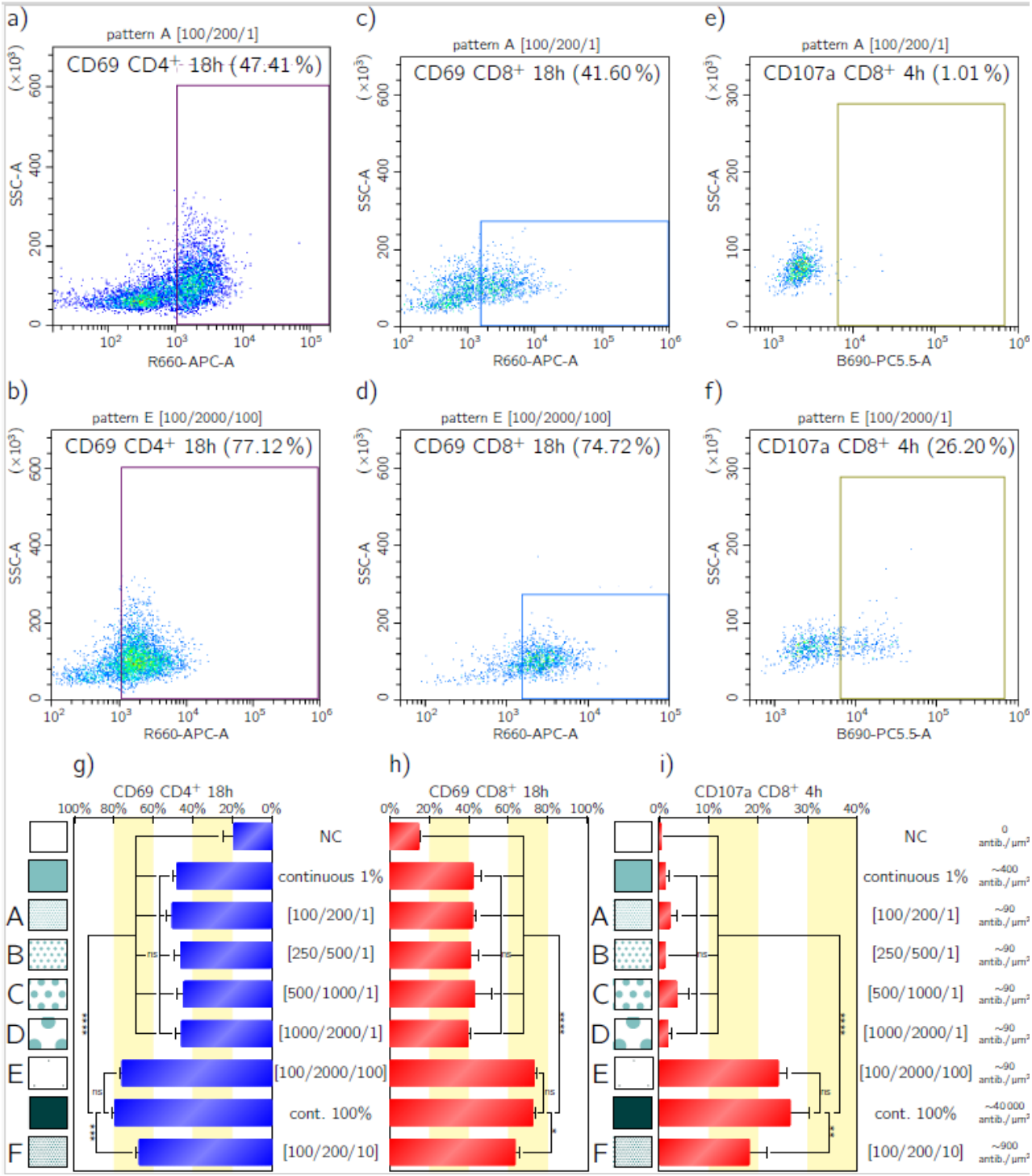

Figure 4. CD4+ and CD8+ activation on different patterned substrates. (a)–(f) Representative examples of flow cytometry measurements for CD69 (a,b) and CD107a (c-f) expression for patterns A [100/200/1] (a,c,e) and E [100/2000/100] (b,d,f). Experimentally measured quantification of CD69 expression for $CD4^+$ (g) and $CD8^+$ (h) cells stimulated on various patterned substrates. (i) Expression of CD107a for $CD8^+$ cells stimulated on various patterned substrates.

We then studied T cell activation on surfaces with co-clustered α-CD3 α-CD28. As in baseline experiments, PBMCs from a healthy donor were plated on antibody-patterned surfaces, fixed, and stained for cytoskeletal and nuclear markers (Fig. 3e). Fluorescence and electron microscopy confirmed T cell spreading, tight contact with clusters, and formation of nanometric protrusions resembling microvilli[32,33]. Activation was assessed by CD69 (18 h) and CD107a (4 h) expression via flow cytometry (Fig. 4a–f), with PEG-coated gold as a negative control. Patterns A–D, despite presenting many 100 nm clusters, showed minimal CD69 expression—similar to low-density continuous coatings—indicating no clustering compensation at this global density. In contrast, pattern E, featuring small, widely spaced but tightly packed clusters, significantly increased CD69 expression in both CD4+ and CD8+ cells (Fig. 4g,h), outperforming even pattern F, which had tenfold higher antibody density. In fact, pattern E's activation level approached that of densely coated homogeneous surfaces.

The interplay between global α-CD3/α-CD28 density and clustering is even more pronounced when examining CD107a. The difference between the A–D and E configurations resulted in more than a tenfold increase in the percentage of $CD8^+$ cells expressing CD107a (Fig. 4i), providing a level of activation larger than pattern F, and not showing significant differences to a continuous, fully packed surface. This demonstrates that while a low global antibody density may be insufficient for full T cell activation when antibodies are randomly distributed, confining them into dense clusters can compensate for this limitation. Furthermore, this shows that the size of the cluster is not definitive for T cell activation but that it is enough to create a small number of stable bindings.

It is noteworthy that here, as in our previous work,[34] we used PBMCs, which, in addition to primary T cells, also contain various amounts of NK cells, APCs and B cells. However, both our continuous array and patterned surfaces were coated with α-CD3/α-CD28, and were therefore T cell-specific, thus ensuring a minimal effect of these surfaces on other cell types present in the PBMC population. This, in turn, ensured a minimal impact of other cell types on T cells across different used activation surfaces. This is confirmed by the consistently significant differences in CD69 and CD107a levels between surfaces with and without α-CD3/α-CD28, thus ensuring the negligible effect of other cell types on the CD69 and CD107a signals produced by T cells.

These observations can be rationalized by adapting the so-called Membrane Fluctuation Model (MFM) for immune cell activation (Fig. 5a) originally conceived for natural killer cells.[28,35] In essence, MFM captures the dynamic coupling between the ligand–receptor binding and the activity of the cell through a mechanical feedback (Fig. 5b), while the rates for binding and unbinding directly depend on the proximity of neighboring ligand(antibody) –receptor constructs. The model assumes that the activation is proportional to the density $\boldsymbol{\mathcal{N}}$ of ligand–receptor bonds of the cell, which, in the stationary state, is given by $\boldsymbol{\mathcal{N}} = \boldsymbol{\varrho}\overline{\boldsymbol{K}_{\mathrm{on}}}/(\overline{\boldsymbol{K}_{\mathrm{off}}} + \overline{\boldsymbol{K}_{\mathrm{on}}})$, with $\boldsymbol{\varrho}$ denoting antibody density, and $\overline{\boldsymbol{K}_{\mathrm{on}}}$ and $\overline{\boldsymbol{K}_{\mathrm{off}}}$ being average binding and unbinding rates, respectively. These average rates are calculated from the first principles assuming

bonds to be springs with defined stiffness and rest length (see SI for details), while the averaging is performed over possible surface binding sites and bond distributions.[36]

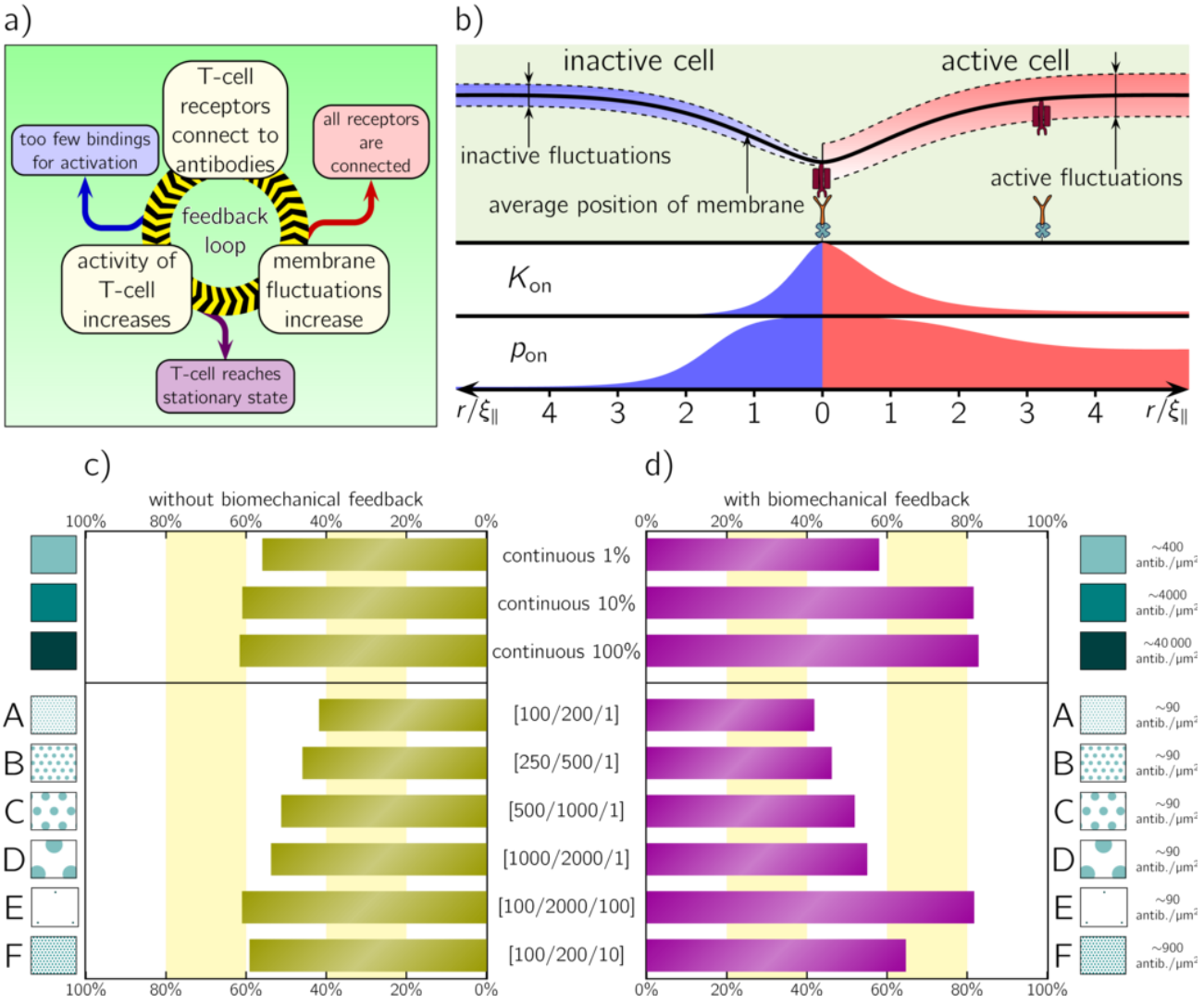

Figure 5. a) Schematic plot of the biomechanical feedback loop in Membrane Fluctuation Model. Binding of receptors on the membrane of T cell is increasing activity of the cell and, as a result, membrane fluctuations are increasing which promotes further binding. b) Schematic comparison of the binding process for inactive (left side) and active cell (right side). For active cell the fluctuations of the membrane are stronger (as illustrated in top part of the scheme). As a result, both binding rate K_{on} and probability p_{on} of binding of next receptor is increased. c) Numerical simulations of activity of cell assuming there is no biomechanical feedback (and thus only inactive fluctuations are present) for continuous arrays (top part) and for all the patterns presented in Fig. 3a. d) The same results as on panel c) but with the mechanism of biomechanical feedback increasing the cell membrane fluctuations.

MFM was first applied to homogeneous antibody distributions, showing that T cell signaling

increases with global antibody density (Fig. 5c,d, top). However, only when mechanical feedback was included—linking cell activity to the fraction of bound antibodies rather than average density—did the model align qualitatively with experimental results (see SI for a more detailed discussion). The lowest probed density of ~400 antibodies/μm^2 produced the lowest percentage of bounded receptors, which initiated partial biomechanical feedback and could not induce full activation. Yet, the activity of the cell increases between ~400 and ~4000 antibodies/μm^2, until it reaches saturation between ~4000 and 40 000 antibodies/μm^2. This highlights the fact that activation is indeed a process in which the dynamic evolution of the number of formed bonds influences the state of the cell and consequently, the state of the membrane. We, furthermore, conclude that undiluted arrays provide an excess amount of activating and costimulatory signal.[37]

Encouraged by this agreement, we applied the MFM model to patterned surfaces (Fig. 5c,d, bottom). As in experiments, diluted patterns failed to trigger mechanical feedback, while dense clustering of antibodies—even at low global densities—enhanced binding rates and bond stability, activating T cells through a proximity-driven feedback loop (Fig. 5b). MFM shows that the binding and unbinding rates (K_{on}, K_{off} respectively) are directly coupled to the membrane configuration and are explicit functions of the average height and the fluctuation amplitude, while the latter increases with the cell activity following a logistic function.[39] Following previous arguments, TCR receptor binding induces transversal proximity between the T cell and a target cell, but away from the bond, the gap between the two membranes is set by the size of large phosphatase molecules.[38–40] This is directly implemented in the MFM model by setting the size of the ligand–receptor bond and the parametrization of the gap. MFM model shows that both the deformation of the membrane due to antibody binding and the change of fluctuations due to change in activity is necessary to initiate biomechanical feedback.

The result is strongly increased binding close to an existing bond in a transversal proximity of about 40 nm[41,42] due to the finite lateral correlation length of the membrane.[43] This further facilitates the formation of more similarly sized ligand–receptor bonds around already formed bonds.[44] The accumulation of these bonds can counteract the repulsive forces between the membranes, further stabilizing the bonds, even in an activated state.[45] The formation of bonds triggers the signaling and initiates the activation process, which, in turn, changes the state of the cell, enhancing the cytoskeleton dynamics, cytoplasmic flows and/or ion channel activity among other processes. The ensemble of these processes boosts the dynamics of the membrane, which is reflected in increasing fluctuation amplitudes with activation.[25,39] In turn, a change in membrane fluctuations leads to changes in the binding and unbinding rates, hence serving as mechanical feedback. Nearby receptors on the membrane are affected in a geometry-dependent manner, yielding strong correlations that promote further binding. Hence, the amplification process ensues until the number of bonds and the activity of the cell saturates in a new steady state. Therefore, even though a certain global antibody density

could be insufficient for full T cell activation if the antibodies are randomly distributed over the surface, a compensatory effect can be achieved at the same density if the antibodies are grouped into clusters. Interestingly, these small cluster sizes and large periodicity mimic the ligand–receptor nanoclusters observed at the physiological interface between T cells and target cells.[46]

In summary, our study demonstrates that clustering plays a central role in regulating T cell activation, particularly at low ligand or antibody densities—a finding well accounted for by the membrane fluctuation model. This model highlights membrane elasticity as a key contributor to the clustering mechanism while integrating the well-established increase in cytoskeletal dynamics in activation. The resulting rapid actin remodeling, cytoplasmic flows, and enhanced membrane trafficking significantly modulate membrane fluctuations, owing to the membrane's low bending stiffness. A critical next step will be to directly correlate T cell binding dynamics with quantitative measurements of membrane state. Experimentally, this could be done, for instance, by combining dynamic optical displacement spectroscopy with super-resolution microscopy, alongside precise control of photobleaching. An alternative approach could involve reflection interference contrast microscopy operated in dynamic fluctuation mode; however, without accounting for the evolution of the refractive index, this method would only provide relative amplitude measurements. Although such simultaneous measurements present substantial technical challenges, they remain a crucial objective for future work, as they would provide definitive evidence of the role of cell mechanics in T cell activation.

Additional research should, furthermore, combine clustering with additional mechanical cues, such as the viscoelasticity[47–50] and nanoscale topography[51,52–54] of the surface to which the molecules are tethered. This is possible by using reductionist platforms that controllably alter each of these parameters[55] while combining them with patterning methods,[26,56–59] which today are achieving control at the individual molecule level.[60–62] Such sophisticated platforms will offer valuable insights into the forces exerted by cells and their correlation with immune responses. This will lay the foundation for optimizing mechanical stimuli and drive significant progress in understanding the physical mechanisms underlying T cell activation.

We believe that, beyond providing insights into the fundamental mechanisms of T cell activation, our findings pave the way for the development of next-generation T cell priming platforms for clinical applications, such as adoptive T cell transfer and Chimeric Antigen Receptor (CAR) T cell immunotherapy. Current T cell priming approaches—such as those based on beads coated with activating and costimulatory antibodies—deliver a maximal dose of stimulation due to the uncontrolled and dense distribution of surface-bound antibodies. However, it is increasingly evident that excessive stimulation does not necessarily yield optimal antitumor potency[63], as overstimulation can lead to rapid T cell exhaustion. By further exploring the strategy of tuning activation through antibody clustering, one could design immunotherapeutic priming platforms in which activating and costimulatory molecules (e.g., receptor-specific ligands or antibodies) are presented in well-defined nanoclusters with controlled size and spacing. According to our findings, this

approach could maintain an overall low stimulus level per T cell while still enabling adequate activation—sufficient for effective transfection with artificial receptors and for expansion to clinically relevant cell numbers—while minimizing exhaustion and prolonging antitumor effects.

Finally, T cell priming platforms could harness this newly generated understanding of the importance of molecular clustering in synergy with other mechanical stimuli. We have already demonstrated that tuning the microtopography and elasticity of the surface enables the production of CAR T cells with antitumor potency exceeding that of T cells generated by standard priming methods, even with excessive concentrations of tethered antibodies.[64] Moving forward, engineering an optimized T cell priming platform, where all physical parameters are precisely orchestrated, offers a promising path toward achieving superior immunotherapeutic outcomes.

Information describing the materials and methods, flow cytometry data, with statistics, showing the impact of antibody surface density on IFNγ, CD69 and CD107a expression, SEM analyses of the nanoarrays as well as details further explaining the Membrane Fluctuation Model is available in the Supporting Information file.

A.-S.S. and M.S. gratefully acknowledge the support of the German Research Foundation *via* Joint Project SM 289/10-1. M.S. acknowledges the support of the Israel Science Foundation Project 2016/21. A.-S.S. and P.N. received further support by the German Science Foundation and the French National Research Agency Project SM 289/8-1.

References

(1) Long, A. H.; Haso, W. M.; Shern, J. F.; Wanhainen, K. M.; Murgai, M.; Ingaramo, M.; Smith, J. P.; Walker, A. J.; Kohler, M. E.; Venkateshwara, V. R.; Kaplan, R. N.; Patterson, G. H.; Fry, T. J.; Orentas, R. J.; Mackall, C. L. 4-1BB Costimulation Ameliorates T Cell Exhaustion Induced by Tonic Signaling of Chimeric Antigen Receptors. *Nat. Med.* **2015**, *21* (6), 581–590. https://doi.org/10.1038/NM.3838.

(2) Waldman, A. D.; Fritz, J. M.; Lenardo, M. J. A Guide to Cancer Immunotherapy: From T Cell Basic Science to Clinical Practice. *Nat. Rev. Immunol.* **2020**, *20* (11), 651–668. https://doi.org/10.1038/s41577-020-0306-5.

(3) Li, R.; Ma, C.; Cai, H.; Chen, W. The CAR T-Cell Mechanoimmunology at a Glance. *Adv. Sci.* **2020**, *7* (24), 2002628. https://doi.org/10.1002/advs.202002628.

(4) Zhang, D. K. Y.; Adu-Berchie, K.; Iyer, S.; Liu, Y.; Cieri, N.; Brockman, J. M.; Neuberg, D.; Wu, C. J.; Mooney, D. J. Enhancing CAR-T Cell Functionality in a Patient-Specific Manner. *Nat. Commun.* **2023**, *14* (1), 506. https://doi.org/10.1038/s41467-023-36126-7.

(5) Huang, J.; Zarnitsyna, V. I.; Liu, B.; Edwards, L. J.; Jiang, N.; Evavold, B. D.; Zhu, C. The Kinetics of Two-Dimensional TCR and pMHC Interactions Determine T-Cell Responsiveness. *Nature* **2010**, *464* (7290), 932–936. https://doi.org/10.1038/nature08944.

(6) Hellmeier, J.; Platzer, R.; Eklund, A. S.; Schlichthaerle, T.; Karner, A.; Motsch, V.; Schneider, M. C.;

Kurz, E.; Bamieh, V.; Brameshuber, M.; Preiner, J.; Jungmann, R.; Stockinger, H.; Schütz, G. J.; Huppa, J. B.; Sevcsik, E. DNA Origami Demonstrate the Unique Stimulatory Power of Single pMHCs as T Cell Antigens. *Proc. Natl. Acad. Sci.* **2021**, *118* (4), e2016857118. https://doi.org/10.1073/pnas.2016857118.

(7) Minguet, S.; Swamy, M.; Alarcón, B.; Luescher, I. F.; Schamel, W. W. A. Full Activation of the T Cell Receptor Requires Both Clustering and Conformational Changes at CD3. *Immunity* **2007**, *26* (1), 43–54. https://doi.org/10.1016/j.immuni.2006.10.019.

(8) Davis, S. J.; van der Merwe, P. A. The Kinetic-Segregation Model: TCR Triggering and Beyond. *Nat. Immunol.* **2006**, *7* (8), 803–809. https://doi.org/10.1038/ni1369.

(9) Choudhuri, K.; Wiseman, D.; Brown, M. H.; Gould, K.; Van Der Merwe, P. A. T-Cell Receptor Triggering Is Critically Dependent on the Dimensions of Its Peptide-MHC Ligand. *Nature* **2005**, *436* (7050), 578–582. https://doi.org/10.1038/nature03843.

(10) Kumari, S.; Curado, S.; Mayya, V.; Dustin, M. L. T Cell Antigen Receptor Activation and Actin Cytoskeleton Remodeling. *Biochim. Biophys. Acta BBA - Biomembr.* **2014**, *1838* (2), 546–556. https://doi.org/10.1016/j.bbamem.2013.05.004.

(11) Krogsgaard, M.; Davis, M. M. How T Cells "see" Antigen. *Nat. Immunol.* **2005**, *6* (3), 239–245. https://doi.org/10.1038/ni1173.

(12) Roh, K.-H.; Lillemeier, B. F.; Wang, F.; Davis, M. M. The Coreceptor CD4 Is Expressed in Distinct Nanoclusters and Does Not Colocalize with T-Cell Receptor and Active Protein Tyrosine Kinase P56lck. *Proc. Natl. Acad. Sci.* **2015**, *112* (13), E1604–E1613. https://doi.org/10.1073/pnas.1503532112.

(13) Pageon, S. V.; Tabarin, T.; Yamamoto, Y.; Ma, Y.; Bridgeman, J. S.; Cohnen, A.; Benzing, C.; Gao, Y.; Crowther, M. D.; Tungatt, K.; Dolton, G.; Sewell, A. K.; Price, D. A.; Acuto, O.; Parton, R. G.; Gooding, J. J.; Rossy, J.; Rossjohn, J.; Gaus, K. Functional Role of T-Cell Receptor Nanoclusters in Signal Initiation and Antigen Discrimination. *Proc. Natl. Acad. Sci.* **2016**, *113* (37), E5454–E5463. https://doi.org/10.1073/pnas.1607436113.

(14) Yokosuka, T.; Saito, T. Dynamic Regulation of T-Cell Costimulation through TCR-CD28 Microclusters. *Immunol. Rev.* **2009**, *229* (1), 27–40. https://doi.org/10.1111/j.1600-065X.2009.00779.x.

(15) Varma, R.; Campi, G.; Yokosuka, T.; Saito, T.; Dustin, M. L. T Cell Receptor-Proximal Signals Are Sustained in Peripheral Microclusters and Terminated in the Central Supramolecular Activation Cluster. *Immunity* **2006**, *25* (1), 117–127. https://doi.org/10.1016/j.immuni.2006.04.010.

(16) Schamel, W. W. A.; Alarcón, B. Organization of the Resting TCR in Nanoscale Oligomers. *Immunol. Rev.* **2013**, *251* (1), 13–20. https://doi.org/10.1111/imr.12019.

(17) Smith, A.-S.; Sengupta, K.; Goennenwein, S.; Seifert, U.; Sackmann, E. Force-Induced Growth of Adhesion Domains Is Controlled by Receptor Mobility. *Proc. Natl. Acad. Sci.* **2008**, *105* (19), 6906–6911. https://doi.org/10.1073/pnas.0801706105.

(18) Dillard, P.; Varma, R.; Sengupta, K.; Limozin, L. Ligand-Mediated Friction Determines Morphodynamics of Spreading T Cells. *Biophys. J.* **2014**, *107*, 2629–2638. https://doi.org/10.1016/j.bpj.2014.10.044.

(19) Adu-Berchie, K.; Mooney, D. J. Biomaterials as Local Niches for Immunomodulation. *Acc. Chem. Res.* **2020**, *53* (9), 1749–1760. https://doi.org/10.1021/acs.accounts.0c00341.

(20) Cheung, A. S.; Zhang, D. K. Y.; Koshy, S. T.; Mooney, D. J. Scaffolds That Mimic Antigen-Presenting Cells Enable Ex Vivo Expansion of Primary T Cells. *Nat. Biotechnol.* **2018**, *36* (2), 160–169. https://doi.org/10.1038/nbt.4047.

(21) Schluck, M.; Hammink, R.; Figdor, C. G.; Verdoes, M.; Weiden, J. Biomaterial-Based Activation and Expansion of Tumor-Specific T Cells. *Front. Immunol.* **2019**, *10* (MAY). https://doi.org/10.3389/FIMMU.2019.00931.

(22) Han, B.; Song, Y.; Park, J.; Doh, J. Nanomaterials to Improve Cancer Immunotherapy Based on Ex Vivo Engineered T Cells and NK Cells. *J. Control. Release Off. J. Control. Release Soc.* **2022**, *343*, 379–391. https://doi.org/10.1016/j.jconrel.2022.01.049.

(23) Rossboth, B.; Arnold, A. M.; Ta, H.; Platzer, R.; Kellner, F.; Huppa, J. B.; Brameshuber, M.;

Baumgart, F.; Schütz, G. J. TCRs Are Randomly Distributed on the Plasma Membrane of Resting Antigen-Experienced T Cells. *Nat. Immunol.* **2018**, *19* (8), 821–827. https://doi.org/10.1038/s41590-018-0162-7.

(24) Sengupta, K.; Dillard, P.; Limozin, L. Morphodynamics of T-Lymphocytes: Scanning to Spreading. *Biophys. J.* **2024**. https://doi.org/10.1016/j.bpj.2024.02.023.

(25) Goyette, J.; Nieves, D. J.; Ma, Y.; Gaus, K. How Does T Cell Receptor Clustering Impact on Signal Transduction? *J. Cell Sci.* **2019**, *132* (4), jcs226423. https://doi.org/10.1242/jcs.226423.

(26) Matic, J.; Deeg, J.; Scheffold, A.; Goldstein, I.; Spatz, J. P. Fine Tuning and Efficient T Cell Activation with Stimulatory aCD3 Nanoarrays. *Nano Lett.* **2013**, *13* (11), 5090–5097. https://doi.org/10.1021/nl4022623.

(27) Delcassian, D.; Depoil, D.; Rudnicka, D.; Liu, M.; Davis, D. M.; Dustin, M. L.; Dunlop, I. E. Nanoscale Ligand Spacing Influences Receptor Triggering in T Cells and NK Cells. *Nano Lett.* **2013**, *13* (11), 5608–5614. https://doi.org/10.1021/nl403252x.

(28) Pandey, A.; Nowakowski, P.; Ureña Martin, C.; Abu Ahmad, M.; Edri, A.; Toledo, E.; Tzadka, S.; Walther, J.; Le Saux, G.; Porgador, A.; Smith, A.-S.; Schvartzman, M. Membrane Fluctuation Model for Understanding the Effect of Receptor Nanoclustering on the Activation of Natural Killer Cells through Biomechanical Feedback. *Nano Lett.* **2024**, *24* (18), 5395–5402. https://doi.org/10.1021/acs.nanolett.3c02815.

(29) Hinrichsen, E. L.; Feder, J.; Jøssang, T. Random Packing of Disks in Two Dimensions. *Phys. Rev. A* **1990**, *41* (8), 4199–4209. https://doi.org/10.1103/PhysRevA.41.4199.

(30) Agheli, H.; Malmström, J.; Larsson, E. M.; Textor, M.; Sutherland, D. S. Large Area Protein Nanopatterning for Biological Applications. *Nano Lett.* **2006**, *6* (6), 1165–1171. https://doi.org/10.1021/nl060403i.

(31) Tzadka, S.; Ureña Martin, C.; Toledo, E.; Yassin, A. A. K.; Pandey, A.; Le Saux, G.; Porgador, A.; Schvartzman, M. A Novel Approach for Colloidal Lithography: From Dry Particle Assembly to High-Throughput Nanofabrication. *ACS Appl. Mater. Interfaces* **2024**, *16* (14), 17846–17856. https://doi.org/10.1021/acsami.3c18554.

(32) Jung, Y.; Riven, I.; Feigelson, S. W.; Kartvelishvily, E.; Tohya, K.; Miyasaka, M.; Alon, R.; Haran, G. Three-Dimensional Localization of T-Cell Receptors in Relation to Microvilli Using a Combination of Superresolution Microscopies. *Proc. Natl. Acad. Sci.* **2016**, *113* (40), E5916–E5924. https://doi.org/10.1073/pnas.1605399113.

(33) Razvag, Y.; Neve-Oz, Y.; Sajman, J.; Reches, M.; Sherman, E. Nanoscale Kinetic Segregation of TCR and CD45 in Engaged Microvilli Facilitates Early T Cell Activation. *Nat. Commun.* **2018**, *9* (1), 732. https://doi.org/10.1038/s41467-018-03127-w.

(34) Pandit, J. J.; Yassin, A. A.-K.; Martin, C. U.; Saux, G. L.; Porgador, A.; Schvartzman, M. Effect of Binary Mechanical Environment on T Cell Function. *Acta Biomater.* **2025**, *195*, 83–93. https://doi.org/10.1016/j.actbio.2025.02.029.

(35) Toledo, E.; Le Saux, G.; Edri, A.; Li, L.; Rosenberg, M.; Keidar, Y.; Bhingardive, V.; Radinsky, O.; Hadad, U.; Di Primo, C.; Buffeteau, T.; Smith, A.-S.; Porgador, A.; Schvartzman, M. Molecular-Scale Spatio-Chemical Control of the Activating-Inhibitory Signal Integration in NK Cells. *Sci. Adv.* **2021**, *7* (24), eabc1640. https://doi.org/10.1126/sciadv.abc1640.

(36) Janeš, J. A.; Monzel, C.; Schmidt, D.; Merkel, R.; Seifert, U.; Sengupta, K.; Smith, A.-S. First-Principle Coarse-Graining Framework for Scale-Free Bell-Like Association and Dissociation Rates in Thermal and Active Systems. *Phys. Rev. X* **2022**, *12* (3), 031030. https://doi.org/10.1103/PhysRevX.12.031030.

(37) Schodin, B. A.; Tsomides, T. J.; Kranz, D. M. Correlation Between the Number of T Cell Receptors Required for T Cell Activation and TCR–Ligand Affinity. *Immunity* **1996**, *5* (2), 137–146. https://doi.org/10.1016/S1074-7613(00)80490-2.

(38) Bruinsma, R.; Behrisch, A.; Sackmann, E. Adhesive Switching of Membranes: Experiment and Theory. *Phys. Rev. E Stat. Phys. Plasmas Fluids Relat. Interdiscip. Top.* **2000**, *61* (4 Pt B), 4253–4267. https://doi.org/10.1103/physreve.61.4253.

(39) Sackmann, E.; Smith, A.-S. Physics of Cell Adhesion: Some Lessons from Cell-Mimetic Systems.

Soft Matter **2014**, *10* (11), 1644–1659. https://doi.org/10.1039/C3SM51910D.
(40) Weikl, T. R.; Lipowsky, R. Pattern Formation during T-Cell Adhesion. *Biophys. J.* **2004**, *87* (6), 3665–3678. https://doi.org/10.1529/biophysj.104.045609.
(41) Allard, J. F.; Dushek, O.; Coombs, D.; Anton Van Der Merwe, P. Mechanical Modulation of Receptor-Ligand Interactions at Cell-Cell Interfaces. *Biophys. J.* **2012**, *102* (6), 1265–1273. https://doi.org/10.1016/j.bpj.2012.02.006.
(42) Dushek, O.; Goyette, J.; van der Merwe, P. A. Non-Catalytic Tyrosine-Phosphorylated Receptors. *Immunol. Rev.* **2012**, *250* (1), 258–276. https://doi.org/10.1111/imr.12008.
(43) Janeš, J. A.; Stumpf, H.; Schmidt, D.; Seifert, U.; Smith, A. S. Statistical Mechanics of an Elastically Pinned Membrane: Static Profile and Correlations. *Biophys. J.* **2019**, *116* (2), 283–295. https://doi.org/10.1016/j.bpj.2018.12.003.
(44) Seifert, U. Vesicles as a Model for Controlled (de-)Adhesion of Cells: A Thermodynamic Approach. *Soft Matter* **2007**, *3*. https://doi.org/10.1039/b611892e.
(45) Janeš, J. A.; Monzel, C.; Schmidt, D.; Merkel, R.; Seifert, U.; Sengupta, K.; Smith, A.-S. First-Principle Coarse-Graining Framework for Scale-Free Bell-Like Association and Dissociation Rates in Thermal and Active Systems. *Phys. Rev. X* **2022**, *12*. https://doi.org/10.1103/PhysRevX.12.031030.
(46) Sherman, E.; Barr, V.; Samelson, L. E. Super-Resolution Characterization of TCR-Dependent Signaling Clusters. *Immunol. Rev.* **2013**, *251* (1), 21–35. https://doi.org/10.1111/imr.12010.
(47) Judokusumo, E.; Tabdanov, E.; Kumari, S.; Dustin, M. L.; Kam, L. C. Mechanosensing in T Lymphocyte Activation. *Biophys J* **2012**, *102*, L5–L7. https://doi.org/10.1016/j.bpj.2011.12.011.
(48) O'Connor, R. S.; Hao, X.; Shen, K.; Bashour, K.; Akimova, T.; Hancock, W. W.; Kam, L. C.; Milone, M. C. Substrate Rigidity Regulates Human T Cell Activation and Proliferation. *J. Immunol. Baltim. Md 1950* **2012**, *189* (3), 1330–1339. https://doi.org/10.4049/jimmunol.1102757.
(49) Mordechay, L.; Le Saux, G.; Edri, A.; Hadad, U.; Porgador, A.; Schvartzman, M. Mechanical Regulation of the Cytotoxic Activity of Natural Killer Cells. *ACS Biomater. Sci. Eng.* **2020**, *7* (1), 122–132. https://doi.org/10.1021/acsbiomaterials.0c01121.
(50) Basu, R.; Whitlock, B. M.; Husson, J.; Le Floc'h, A.; Jin, W.; Oyler-Yaniv, A.; Dotiwala, F.; Giannone, G.; Hivroz, C.; Biais, N.; Lieberman, J.; Kam, L. C.; Huse, M. Cytotoxic T Cells Use Mechanical Force to Potentiate Target Cell Killing. *Cell* **2016**, *165* (1), 100–110. https://doi.org/10.1016/j.cell.2016.01.021.
(51) Aramesh, M.; Stoycheva, D.; Sandu, I.; Ihle, S. J.; Zünd, T.; Shiu, J.-Y.; Forró, C.; Asghari, M.; Bernero, M.; Lickert, S.; Kotowski, M.; Davis, S. J.; Oxenius, A.; Vogel, V.; Klotzsch, E. Nanoconfinement of Microvilli Alters Gene Expression and Boosts T Cell Activation. *Proc. Natl. Acad. Sci.* **2021**, *118* (40), e2107535118. https://doi.org/10.1073/pnas.2107535118.
(52) Le Saux, G.; Bar-Hanin, N.; Edri, A.; Hadad, U.; Porgador, A.; Schvartzman, M. Nanoscale Mechanosensing of Natural Killer Cells Is Revealed by Antigen-Functionalized Nanowires. *Adv. Mater.* **2019**, *31* (4), 1805954. https://doi.org/10.1002/adma.201805954.
(53) Bhingardive, V.; Le Saux, G.; Edri, A.; Porgador, A.; Schvartzman, M. Nanowire Based Guidance of the Morphology and Cytotoxic Activity of Natural Killer Cells. *Small* **2021**, *17* (14), 2007347. https://doi.org/10.1002/smll.202007347.
(54) Rathar, R.; Sanchez-Fuentes, D.; Lachuer, H.; Meire, V.; Boulay, A.; Desgarceaux, R.; Blanchet, F. P.; Carretero-Genevrier, A.; Picas, L. Tuning the Immune Cell Response through Surface Nanotopography Engineering. *Small Sci.* **2024**, *4* (9), 2400227. https://doi.org/10.1002/smsc.202400227.
(55) Adutler-Lieber, S.; Zaretsky, I.; Platzman, I.; Deeg, J.; Friedman, N.; Spatz, J. P.; Geiger, B. Engineering of Synthetic Cellular Microenvironments: Implications for Immunity. *J. Autoimmun.* **2014**. https://doi.org/10.1016/j.jaut.2014.05.003.
(56) Cai, H.; Muller, J.; Depoil, D.; Mayya, V.; Sheetz, M. P.; Dustin, M. L.; Wind, S. J. Full Control of Ligand Positioning Reveals Spatial Thresholds for T Cell Receptor Triggering. *Nat. Nanotechnol.* **2018**, *13*, 610–617. https://doi.org/10.1038/s41565-018-0113-3.
(57) Doh, J.; Irvine, D. J. Immunological Synapse Arrays: Patterned Protein Surfaces That Modulate

Immunological Synapse Structure Formation in T Cells. *Proc Nat Acad Sci USA* **2006**, *103*, 5700–5705.

(58) Deeg, J.; Axmann, M.; Matic, J.; Liapis, A.; Depoil, D.; Afrose, J.; Curado, S.; Dustin, M. L.; Spatz, J. P. T Cell Activation Is Determined by the Number of Presented Antigens. *Nano Lett.* **2013**, *13* (11), 5619–5626. https://doi.org/10.1021/nl403266t.

(59) Keydar, Y.; Le Saux, G.; Pandey, A.; Avishay, E.; Bar-Hanin, N.; Esti, T.; Bhingardive, V.; Hadad, U.; Porgador, A.; Schvartzman, M. Natural Killer Cells' Immune Response Requires a Minimal Nanoscale Distribution of Activating Antigens. *Nanoscale* **2018**, *10* (30), 14651–14659. https://doi.org/10.1039/C8NR04038A.

(60) Schvartzman, M.; Wind, S. J. Robust Pattern Transfer of Nanoimprinted Features for Sub-5-Nm Fabrication. *Nano Lett.* **2009**, *9* (10), 3629–3634. https://doi.org/10.1021/nl9018512.

(61) Schvartzman, M.; Palma, M.; Sable, J.; Abramson, J.; Hu, X.; Sheetz, M. P.; Wind, S. J. Nanolithographic Control of the Spatial Organization of Cellular Adhesion Receptors at the Single-Molecule Level. *Nano Lett.* **2011**, *11* (3), 1306–1312. https://doi.org/10.1021/nl104378f.

(62) Cai, H.; Wolfenson, H.; Depoil, D.; Dustin, M. L.; Sheetz, M. P.; Wind, S. J. Molecular Occupancy of Nanodot Arrays. *ACS Nano* **2016**, *10* (4), 4173–4183. https://doi.org/10.1021/acsnano.5b07425.

(63) Zhang, D. K. Y.; Adu-Berchie, K.; Iyer, S.; Liu, Y.; Cieri, N.; Brockman, J. M.; Neuberg, D.; Wu, C. J.; Mooney, D. J. Enhancing CAR-T Cell Functionality in a Patient-Specific Manner. *Nat. Commun.* **2023**, *14* (1), 506. https://doi.org/10.1038/s41467-023-36126-7.

(64) Yassin, A. A.-K.; Ureña Martin, C.; Le Saux, G.; Pandey, A.; Tzadka, S.; Toledo, E.; Pandit, J. J.; Sherf, T.; Nusbaum, I.; Bhattachrya, B.; Banerji, R.; Greenshpan, Y.; Abu Ahmad, M. A.; Radinsky, O.; Sklartz, M.; Gazit, R.; Elkabets, M.; Ghassemi, S.; Cohen, O.; Schvartzman, M.; Porgador, A. Mechanostimulatory Platform for Improved CAR T Cell Immunotherapy. *Adv. Mater.* **2025**, 2412482. https://doi.org/10.1002/adma.202412482.

Tiny Clusters for Big Impact in T Cell Activation

Supporting Information

Guillaume Le Saux[1,2,†], Piotr Nowakowski[3,†], Esti Toledo[1,2], Sivan Tzdaka[1,2], Shagufta Naaz[1,2], Yuval Segal[1,2], Brit Maman[1,2], Jatin Jawhir Pandit[1,2], Muhammed Iraqi[4], Abed Al-Kader Yassin[4], Angel Porgador[4], Ana-Sunčana Smith[3,5,‡], and Mark Schvartzman[1,2,‡]

[1]*Department of Materials Engineering, Faculty of Engineering, Ben-Gurion University of the Negev, Beer-Sheva 84105, Israel*
[2]*Ilse Katz Institute for Nanoscale Science and Technology, Ben-Gurion University of the Negev, Beer-Sheva 84105, Israel*
[3]*Group for Computational Life Sciences, Division of Physical Chemistry, Ruđer Bošković Institute, 10000 Zagreb, Croatia*
[4]*Department of Microbiology and immunology, and Genetics, Faculty of Health Sciences, Ben-Gurion University of the Negev, Beer-Sheva 84105, Israel*
[5]*PULS Group, Institut für Theoretische Physik, IZNF, Friedrich-Alexander-Universität Erlangen-Nürnberg, 91058 Erlangen, Germany*

[†] Equally contributing authors

[‡] Corresponding authors; e-mail: smith@physik.fau.de, asmith@irb.hr; marksc@bgu.ac.il

Materials and Methods

Fabrication of the arrays. Dense monolayers of 200 nm polystyrene nanoparticles were fabricated to silicon substrates using a previously reported method. Briefly, polystyrene nanoparticles (Polyscience, Inc.) were suspended in 2:1 mixture of water:ethanol, and the solution was slowly dispensed from automatic syringe on the surface of Langmuir–Blodgett through filled with DI water, using a glass skinned positioned on the through barrier at an angle.[1] Larger polystyrene nanoparticles were assembled by mechanical rubbing of particle powder between to PDMS surfaces, and the particle monolayer formed on PDMS was mechanically transferred to silicon using PEI adhesive film.[2] The assembled particles were trimmed to half of their diameter using oxygen plasma etching. Then, a thin film of Ti/Au (1 nm/5 nm) was deposited through the formed polystyrene mask by electron beam evaporation, and liftoff in hot chlorobenzene removed the particle, leaving silicon disks surrounded by Au. For electron-beam patterned arrays, silicon substrates were first coated with Ti/Au (1 nm/5 nm) by electron beam evaporation, and by a film of positive e-beam resist (PMMA, 950 K). The films were then exposed by electron-beam writing tool (EBPG 5150), and developed for 1 minute in MIBK:IPA 1:3 solution. The resulting surfaces consist of arrays of silicon nanodisks surrounded by a gold background.

Biofunctionalization of the arrays. Prior to functionalization, samples were cut into 1x1 cm and were fixed to the underside of a bottomless 96-well plate using PDMS as sealant. In this way, cells could be

directly incubated over the samples and would interact solely with the functionalized arrays. The plates were then treated by UV-ozone (Novascan) to activate the native oxide layer of the silicon nanodisks, which were subsequently functionalized using 3-aminopropyl triethoxysilane (APTES, Merck). For this, samples were incubated 30 min in a 5% ethanolic solution of APTES, followed by 30 min baking at 60°C. The amine terminated nanodisks were then derivatized with biotin by soaking overnight in a 1 mM aqueous solution of biotin N-hydroxysuccinimide ester (NHS-Biotin, ThermoFisher). To minimize nonspecific interactions, the gold background was passivated using a 0.5 mM ethanolic solution of mercapto polyethylene glycol (thiol-PEG3400, Nanocs). The plates underwent a final sterilization step by 1 hour soaking in ethanol and all ensuing steps were performed in a sterile laminar flow using sterile buffers. Green-fluorescent avidin (Neutravidin Oregon Green 488, ThermoFisher), was coupled to the biotin terminated nanodisks by incubation for 90 min at a concentration of 25 μg/mL in phosphate buffered saline (PBS) with 2% bovine serum albumin (BSA). The plates were thoroughly rinsed with PBS containing 0.1% Tween20 (PBST), and then with PBS only. Finally, the samples were biofunctionalized with antibodies by 90 min incubation in a 1:1 mix of biotinylated anti-human CD3 (OKT3 clone) and anti-human CD28 (both from Biolegend) at a concentration of 2 μg/mL in PSB with 2% BSA. Finally, the samples were consecutively washed with PBST and PBS and were directly used for cell experiments.

PBMC isolation and activation. Peripheral blood mononuclear cells (PBMCs) were isolated from fresh blood samples that were taken from an adult volunteer as approved by the Helsinki Ethics Committee (approval no. 0062-23-SOR). Isolation was performed using the FICOL gradient. First, blood was diluted with PBS augmented with 2% fetal bovine serum (FBS), at a 1:1 ratio, then loaded on FICOL gradient, and centrifuged at 16°C at 1200 g (with no breaks or acceleration). The PBMCs were collected as the middle disc and a small portion of the underlying phase but taking care not to withdraw the pellet, washed three times with at least 1:2 ratio of PBS in 2% FBS at room temperature, and sedimented at 500 g. The cells were finally suspended in the final medium in the ratio of 2 mL per 7 mL of collected blood, counted, and diluted with the medium to final concentration of 1×10^6 cells per mL. The cells were then seeded onto the surfaces in the growth medium containing <2% serum and 50 units of IL-2 and left inside incubator to adhere for up to 18 h.

Flow cytometry. For flow cytometry measurements, 50 000 cells were used per well. The cells were stained with respective fluorophore-conjugated antibodies at 1:1000 dilution and incubated for 30 minutes on ice. Thereafter, the cells were washed, and the dead cells were stained with DAPI (1:1000 in PBS). All the samples were analyzed on a CytoFLEX LX flow cytometer (Beckman Coulter). For analysis, the fraction of CD3-positive cells was calculated, and CD3-positive cells were then analyzed for staining with the other antibodies employed for staining. The antibodies used for staining were PE anti-human CD3, FITC anti-human CD4, APC Fire 750 anti-human CD8, APC anti-human CD69, and PerCP-Cy5.5 anti-human CD107a (all from Biolegend).

Fluorescence and scanning electron imaging. Two sets of samples with nanoarrays were biofunctionalized as detailed previously without being mounted in 96-well plates. Instead, they were placed in 24-well plates into which PBMCs were seeded. After incubation overnight, cells were fixed in 4% paraformaldehyde at 4°C for 15 min. One set was used for fluorescent microscopy while the other was dedicated to scanning electron microscopy. For fluorescence, the cells were stained for cytoskeleton using AlexaFluor 555 Phalloidin (ThermoFisher), mounted with DAPI containing medium (Abcam), and imaged with a Zeiss LSM 880 confocal microscope. For the other set, the fixed cells were treated with three successive dips in absolute ethanol for

5 min each, then dried in a critical point dryer, sputtered with a thin layer of gold and imaged using a Verios 460L HRSEM.

Statistics. For the flow cytometry experiments, each condition was prepared in triplicate and cells in each individual well were measured. For gating, antibody-positive population were set against the negative control which consisted of naive PBMCs cultured in standard conditions. Results over the triplicates were then averaged. Statistical analyses were performed using Prism (GraphPad), assuming that the data is normally distributed and homogeneity of variance, ANOVA and Tukey post hoc testing were performed to compare between datasets. Results were considered significant for $p<0.05$.

Impact of antibody surface density on interferon gamma expression

For IFN-γ detection, PBMCs were seeded at a density of 10^6 cells/ml onto the surfaces and stimulated 18 hours. Following incubation, the supernatant was aspirated and centrifuged at 4 ˚C for 10 minutes. The debris-free medium was then collected and used immediately. IFN-γ release intensity was quantified by enzyme-linked immunosorbent assay using the protocol provided by BioLegend. Results are shown in Figure S1. ANOVA as well as a Tukey post hoc test were performed (Table S1).

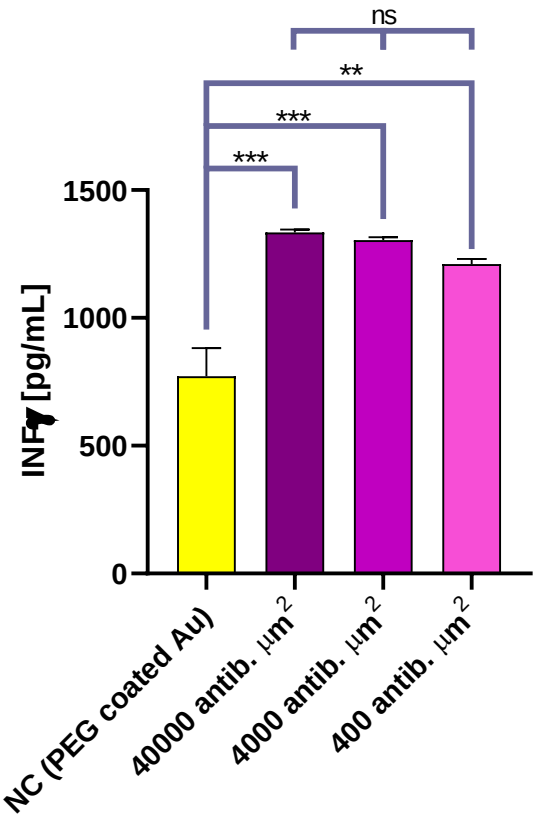

Figure S1. IFNγ secretion by PBMCs on surfaces without and with 400 to 40000 antibodies per μm^2.

Table S1. Statistical analysis. Differences were considered significant for $p<0.05$.

Tukey's multiple comparisons test	Mean Diff.	99.90% CI of diff.	Significant?	Summary	Adjusted P Value
NC (PEG coated Au) vs. 40000 antib. μm^2	−562.3	−1066 to −58.29	Yes	***	0.0005
NC (PEG coated Au) vs. 4000 antib. μm^2	−531.7	−1036 to −27.62	Yes	***	0.0007
NC (PEG coated Au) vs. 400 antib. μm^2	−438.7	−942.7 to 65.38	Yes	**	0.0025
40000 antib. μm^2 vs. 4000 antib. μm^2	30.67	−473.4 to 534.7	No	ns	0.9791
40000 antib. μm^2 vs. 400 antib. μm^2	123.7	−380.4 to 627.7	No	ns	0.4509
4000 antib. μm^2 vs. 400 antib. μm^2	93.00	−411.0 to 597.0	No	ns	0.6597

Impact of antibody surface density on CD69$^+$ expression

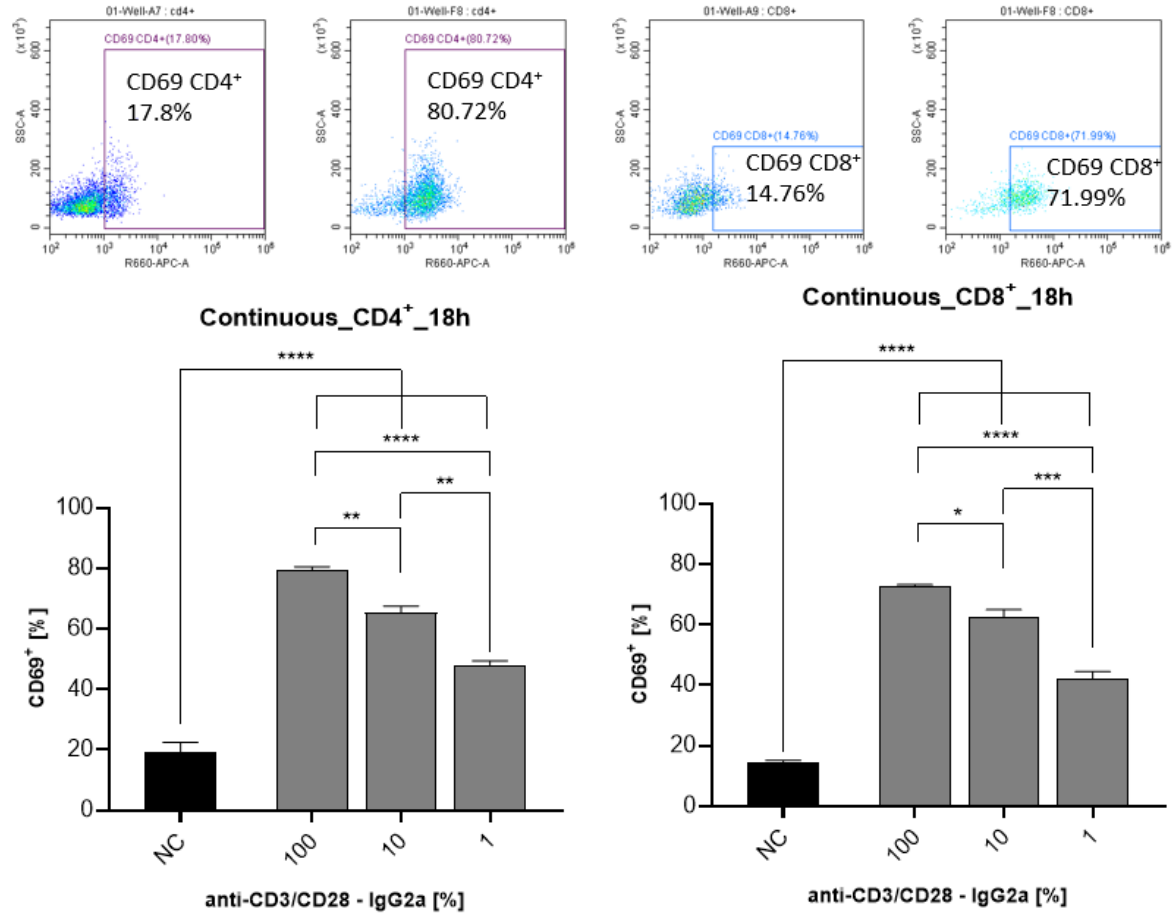

Figure S2. Influence of anti-CD3/CD28 global surface density on T cell activation. Representative dot plots and flow cytometry quantification of CD69$^+$ populations within CD4$^+$ and CD8$^+$ T cells. Continuous surfaces of silicon were modified with various mixes and anti-CD3/CD28 – IgG2a according to the protocol described above. The negative control (NC) consists of PEG modified gold surface. Experiments were performed in triplicate and results were considered significant for $p<0.05$.

Impact of antibody surface density on CD107a$^+$ expression

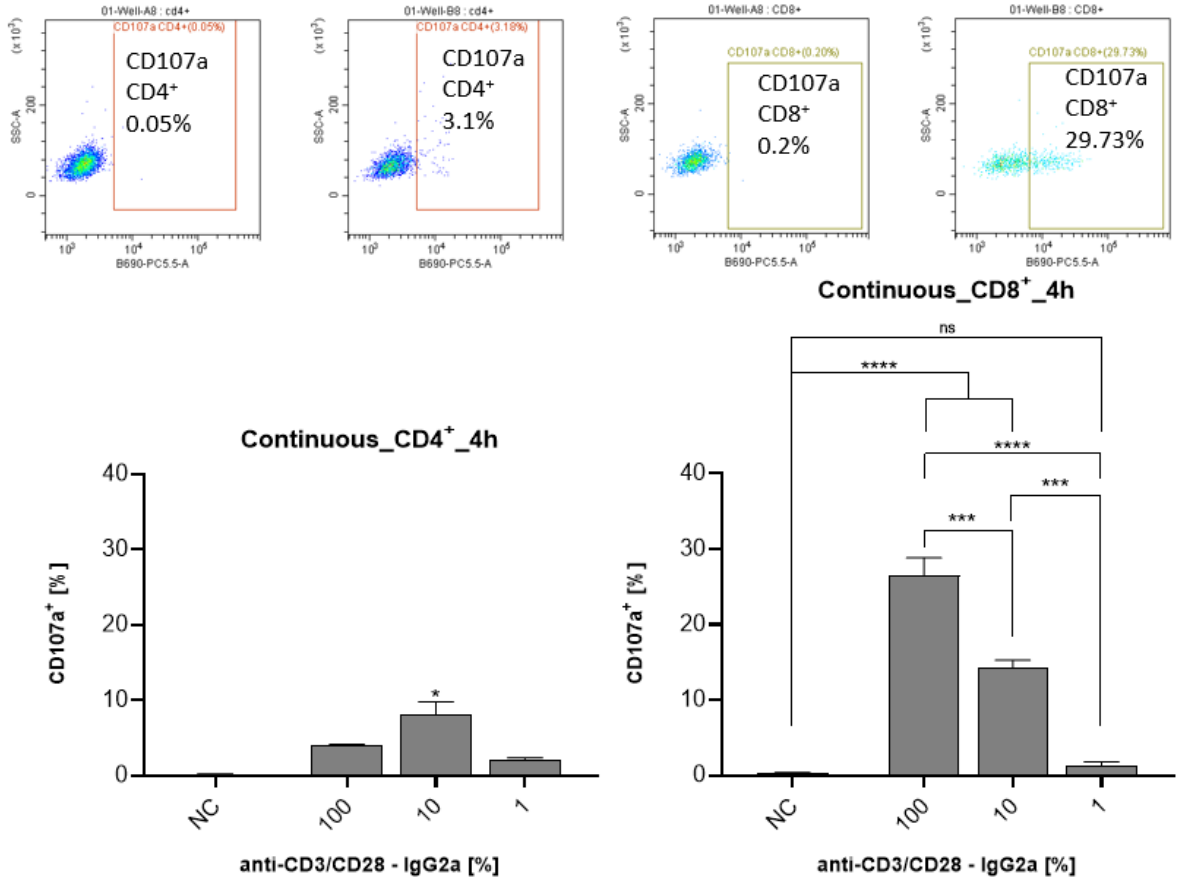

Figure S3. Influence of anti-CD3/CD28 global surface density on T cell degranulation. Representative dot plots and flow cytometry quantification of CD107a$^+$ populations within CD4$^+$ and CD8$^+$ T cells. Continuous surfaces of silicon were modified with various mixes and anti-CD3/CD28 – IgG2a according to the protocol described above. The negative control (NC) consists of PEG modified gold surface. Experiments were performed in triplicate and results were considered significant for $p<0.05$.

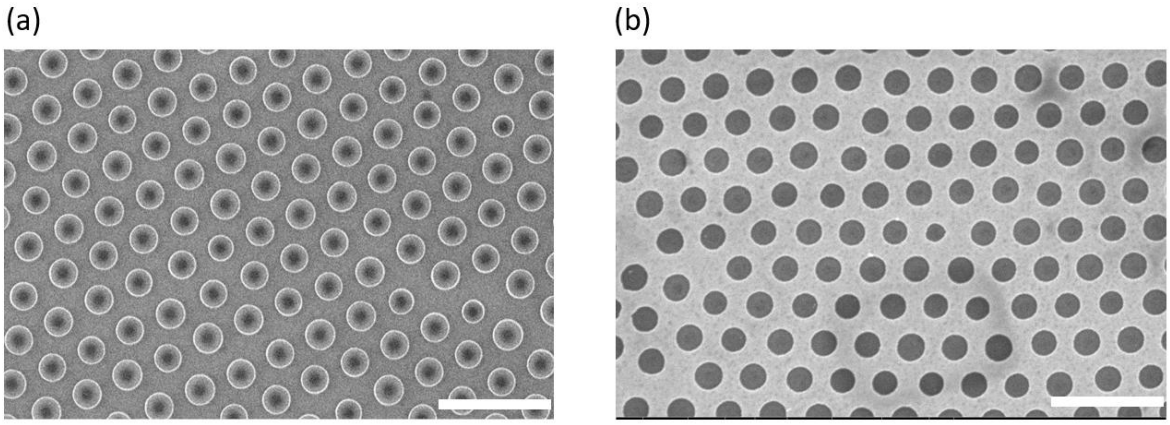

Figure S4: Example of the fabrication results: (a) Array of polystyrene nanospheres with the original diameter of 500 nm, after trimming by Oxygen plasma to half of their original diameter. (b) Array of Silicon disks surrounded by Au mesh obtained after Au deposition and liftoff. Scale bar: 1 μm

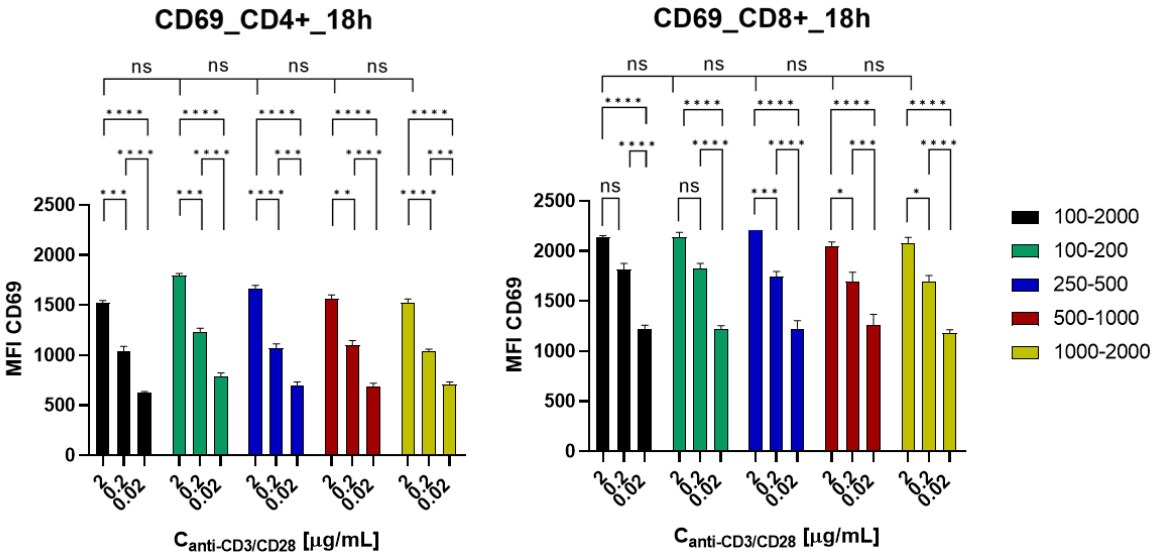

Figure S5: Mean Fluorescence Intensity (MFI) of CD69 expression for CD4+ T cells and CD8+ T cells stimulated on various antibody clusters and dilutions, as obtained by flow cytometry. NC and PC stand for negative and positive controls, respectively. The statistical analysis was performed with Tukey's multiple-comparison tests using the GraphPad Prism software. $*$ $p < 0.05$, $**$ $p < 0.01$, $***$ $p < 0.001$, $****$ $p < 0.0001$, ns: not significant.

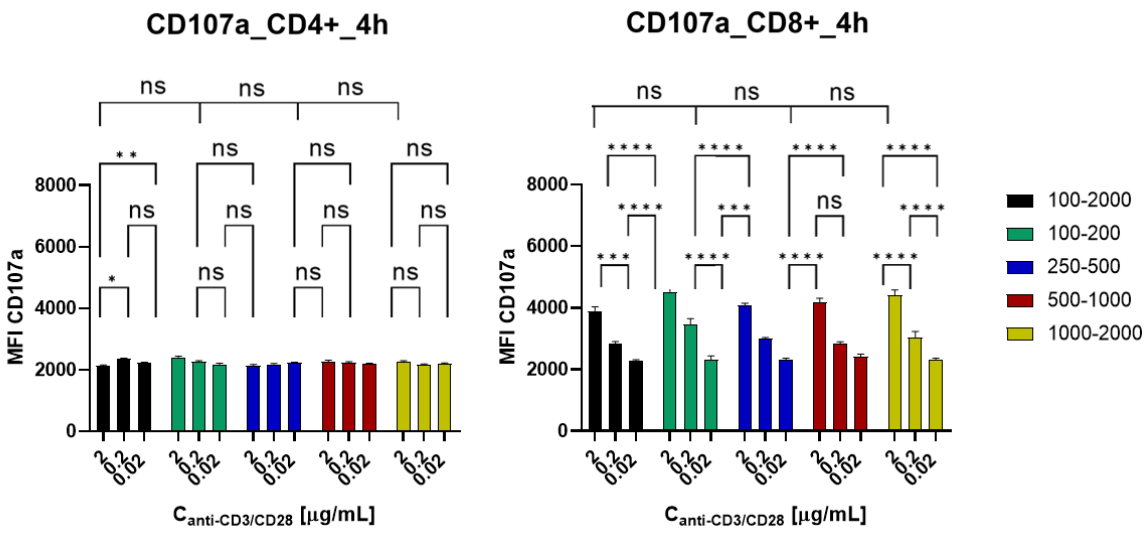

Figure S6: Mean Fluorescence Intensity (MFI) of CD107a expression for CD4+ T cells and CD8+ T cells stimulated on various antibody clusters and dilutions, as obtained by flow cytometry. NC and PC stand for negative and positive controls, respectively. The statistical analysis was performed with Tukey's multiple-comparison tests using the GraphPad Prism software. $* \; p < 0.05$, $** \; p < 0.01$, $*** \; p < 0.001$, $**** \; p < 0.0001$, ns: not significant.

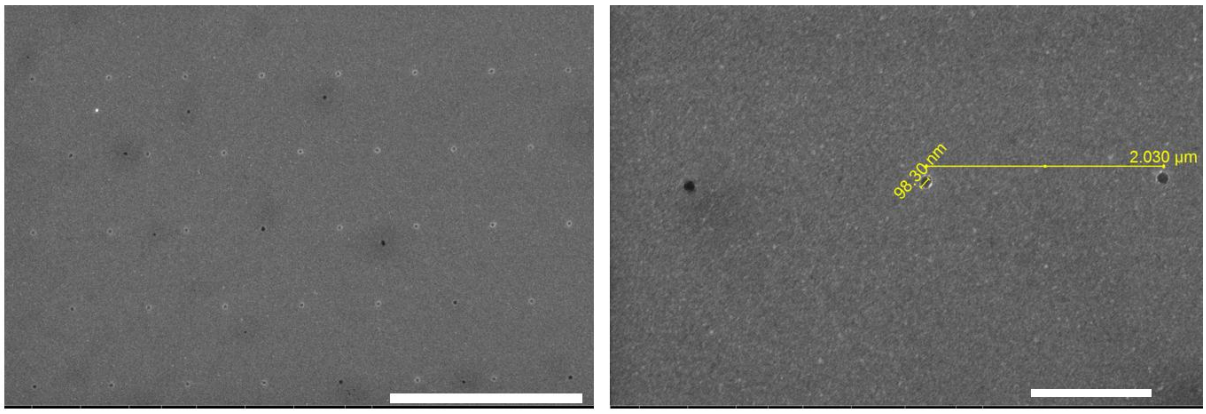

Figure S7: SEM of 100 nm Silicon Dioxide clusters arranged with the spacing of 2 µm. Left: X 8K magnification, scale bar 5 µm, Right: X 25K , scale bar 1 µm.

Membrane fluctuation model

In order to explain the results of experimental measurements we have made calculations using membrane fluctuation model (MFM). This model has already been successfully applied to explain activation of NK cells.[3] In MFM, it is assumed that there is a feedback loop between the number of bonded receptors and the activity of the cell: increasing the number of bindings is increasing activity of the cell which manifest itself by a growth of fluctuations of the membrane, which, in turn, promotes the formation of further bonds.

We describe the membrane by its height over the flat substrate $h(\boldsymbol{r})$, where $\boldsymbol{r}$ is a two-dimensional vector defining a point on the substrate plane. We assume that the energy of each configuration of the membrane is given by a Hamiltonian

$$\mathcal{H}_{\text{membrane}} = \int_{\mathcal{D}} \mathrm{d}\boldsymbol{r} \left[\frac{\kappa}{2}\left(\nabla^2 h(\boldsymbol{r})\right)^2 + \frac{\gamma}{2}\left(h(\boldsymbol{r}) - h_0\right)^2\right] + \frac{\lambda}{2}\sum_{j=1}^{M}\left[h(\boldsymbol{r}_j) - \ell\right]^2, \qquad \text{(S1)}$$

where κ is the bending stiffness of the membrane, γ is the strength of unspecific potential keeping the unbound membrane at the average transversal distance from the patterned surface h_0. The second term in the Hamiltonian (S1) describes interaction of the membrane with M antibodies bound to receptors in positions $\boldsymbol{r}_j$ for $j = 1,2,3,\ldots,M$. Finally, ℓ is the rest length of the antibody-receptor bond that has a stiffness λ. The exact location of antibodies, as well as exact size of a rectangular domain $\mathcal{D}$ of integration, is defined by the pattern on the substrate, as discussed below.

In the MFM, the amplitude of fluctuation of the membrane of an inactive cell σ^{inactive} is increased by the amplitude σ^{active} of fluctuations associated with the activity of the cell. For an inactive cell, which is not bound to antibodies, the membrane hovers at an average transversal distance h_0 from the patterned surface with the Gaussian fluctuations with a standard deviation $\sigma^{\text{inactive}} = \langle(h(\boldsymbol{r}) - h_0)^2\rangle^{1/2} = (64\kappa\gamma)^{-1/4}$.

Upon binding, the activity of the cell may change, giving rise to another component of fluctuations σ^{active} which could enhance the dynamics of the membrane. MFM assumes the relation between σ^{active} and the activity $\mathcal{P}$ in a form of a logistic curve:

$$\sigma^{\text{active}}(\mathcal{P}) = \frac{1}{2}\sigma_{\text{max}}\left[\tanh\left(\frac{\mathcal{P} - \mathcal{P}_0}{\mathcal{P}_{\text{w}}}\right) + 1\right]. \qquad \text{(S2)}$$

Here, the parameters of the model are σ_{max} which denotes the maximal amplitude of active fluctuations, $\mathcal{P}_0$ is the middle value of activity, and $\mathcal{P}_{\text{w}}$ is the width of the sigmoid curve.

Typically, upon the formation of first bonds, a laterally dependent height and fluctuation profile develops.[4] This means that, in reality, every antibody experiences a different average height and fluctuation amplitude σ_j, depending on the evolution of the bonds in its vicinity, yielding correlations between binding events. In MFM the fluctuations of the membrane are assumed to be a convolution of inactive and active fluctuations, and hence, total fluctuation amplitude of the membrane at the position of the antibody is

$$\sigma_j = \left[\left(\sigma_j^{\text{inactive}}\right)^2 + \left(\sigma^{\text{active}}\right)^2\right]^{1/2}. \qquad \text{(S3)}$$

For a given pattern of bound antibodies average height and fluctuation amplitude $\sigma_j^{\text{inactive}}$ can be calculated from Hamiltonian (S1) using the method of path integral.

The fluctuation amplitude and the transversal distance of the membrane from the patterned array both explicitly enter the rates.[5] Consequently, one should calculate binding and unbinding rates K_{on} and K_{off} rates for each antibody j. Notably, these rates should carry the information of the likelihood of finding a receptor in the binding range of the antibody.

Finally, by knowing the rates, one can calculate the activity of the cell, which is assumed to be related to the number of formed bonds $\mathcal{N}$ in stationary state given by

$$\mathcal{N} = \varrho\overline{K_{\mathrm{on}}}/(\overline{K_{\mathrm{off}}} + \overline{K_{\mathrm{on}}}). \quad \text{(S4)}$$

Here, ϱ is the total density of antibodies, and $\overline{K_{\mathrm{on}}}$ and $\overline{K_{\mathrm{off}}}$ denote average binding and unbinding rates, respectively. We approximate $\overline{K_{\mathrm{on}}}$ and $\overline{K_{\mathrm{off}}}$ as a sum of all K_{on} and K_{off} rates calculated for all antibodies within a unit area. However, because of the large number of configurations, calculating these averages is very challenging. We therefore, estimate the average rates by considering only the most probable scenarios: $\overline{K_{\mathrm{on}}}$ is calculated as a rate of binding of the receptors to an antibody from a fully unbound membrane, and $\overline{K_{\mathrm{off}}}$ is calculated as the rate of bond breaking in a fully bound cluster.

Naturally, this approach provides only an approximation of the correlations in the system. Furthermore, we sent the likelihood of finding a receptor above the antibody to unity. To compensate for these approximations, we define the activity of the cell as $\mathcal{P} = \mathcal{N}/\varrho$:

$$\mathcal{P} = \overline{K_{\mathrm{on}}}/(\overline{K_{\mathrm{off}}} + \overline{K_{\mathrm{on}}}). \quad \text{(S5)}$$

Consequently, σ^{active} is enhanced for low densities of antibodies where the collective binding may be of importance, and reduced for larger densities where the limited number of receptors is relevant. This is clearly different from the original application of MFM[3] (where the activity of cell was related to $\mathcal{N}$), in which the densities of ligands on the substrate were not exceeding 250 ligands/μm^2 and were much lower than densities of up to 9000 antibodies/μm^2 present in the current experiment for undiluted antibodies. This guaranteed larger distances between ligands, smaller total densities of bonds, and the number of receptors available on the cell membrane was not a limiting factor. As a result, both of the effects described above were not relevant, and explicit density dependence was maintained. Notably, for our calculations of cell activity at low densities (1% dilution, low and high level of clustering), both approaches provide the same conclusions, as the overall density ϱ is identical in systems that are being compared.

In the calculations without a feedback, we assume the fluctuations to be only inactive by taking $\sigma^{\mathrm{active}} = 0$, regardless of the value of $\mathcal{P}$. For the calculations with the feedback loop we calculate σ^{active} from the sigmoid relation (S2) and increase the fluctuations of the membrane following Eq. (S3). This yields new $\overline{K_{\mathrm{off}}}$ and $\overline{K_{\mathrm{on}}}$, and update in the cell activity $\mathcal{P}$, and consequently a new σ^{active}, until the steady state is achieved. The results are presented in Fig. 3b and Fig. 4b of the main text.

The sigmoid curve (S2) has been fitted graphically to make the feedback loop mechanism work most efficient for moderate densities of antibodies (dilution 10%). While this naturally, overemphasizes the correlations in this range of parameters, as seen in experiments, it provides a good response at the density extremes (no dilution and dilution to 1%), as argued above. The numerical values of all the parameters used in our calculations are presented in Table S2.

Table S2: Numerical values of parameters used in calculations.

name of parameter	symbol	value used in calculations
strength of potential acting on the membrane	γ	$4 \times 10^5\ k_\mathrm{B}T/\mu\mathrm{m}^4$
equilibrium height of the membrane	h_0	80 nm
bending stiffness of the membrane	κ	$30\ k_\mathrm{B}T$
length of bond coupling	ℓ	40 nm
bond spring constant	λ	$2.5 \times 10^4\ k_\mathrm{B}T/\mu\mathrm{m}^2$
binding pocked on the receptor	α	10 nm
intrinsic affinity of bond	ε_b	$9\ k_\mathrm{B}T$
maximum of active fluctuations	σ_max	5 nm
half fluctuation density	$\mathcal{P}_0$	0.715
width of activity curve	$\mathcal{P}_\mathrm{w}$	0.19
diameter of antibody	d_antibody	5 nm

Patterned substrate

In order to model the experimental system of a pattern consisting of circles of the diameter d, forming a hexagonal lattice with spacing p with antibodies attached only inside the circles with a dilution c, we have used the following protocol: First, we set the system shape $\mathcal{D}$ to be a rectangle with periodic boundary conditions (see top row of Fig. 3 in the main text). We choose the width and height of it to be the smallest possible integer multiple of p and $\frac{\sqrt{3}}{2}p$, respectively, for which both width and height are not smaller than $5\xi_\parallel$, where $\xi_\parallel = (\kappa/\gamma)^{1/4}$ is the membrane correlation length in the direction parallel to the substrate. This way we ensure that the periodic boundary conditions do not affect the calculations significantly. Second, we place circles of diameter d in the domain $\mathcal{D}$ to form a hexagonal lattice. Antibodies are placed on a regular square pattern with a spacing d_antibody equal to their typical size. In the third step, we remove the antibodies that do not lay inside the circles forming a hexagonal lattice. Finally, we include the dilution c of active antibodies by removing each antibody with a probability $1 - c$. This way we determined the number of antibodies M and their locations $\boldsymbol{r}_j$ within the domain $\mathcal{D}$. These parameters were then used in Hamiltonian (S1) for further calculations as described in the previous subsection.

We note that while for a system with 100% dilution of active antibodies, pattern of antibodies generated by the above method is fully deterministic, for smaller dilutions the exact locations of antibodies are subject to randomness. For this reason, for each system with a dilution $c < 100\%$ we have repeated the calculation of the percentage of bound antibodies several (not less than 10) times. In the main text we present averages of these calculations and, as we have checked, the dispersion of the results was in each case below the resolution of our graphs.

In special case of the positive control (PC) patterns, where the whole substrate is covered by antibodies, we have taken $\mathcal{D}$ to be a square of the size $5\xi_\parallel$ and we have skipped the third step of the protocol of placing antibodies described above.

In order to keep the computational time reasonable, we have decided to treat separately the special

pattern with $d = 1000\,\mathrm{nm}$, $p = 2000\,\mathrm{nm}$, and $c = 100\%$. In this case, the distance between circles forming hexagonal pattern exceeds $5\xi_{\parallel}$. We have, therefore considered an infinite system ($\mathcal{D} = \mathbb{R}^2$) with a single circle of active antibodies of the radius d in the origin, rather than periodic boundary conditions. This greatly reduced the computation time, for the price of ignoring possible correlations on the membrane at distances larger than 10 correlation lengths. According to previous calculations,[4] this should not affect the obtained results.

Bibliography

[1] Thangamuthu, M.; Santschi, C.; Martin, O. Reliable Langmuir Blodgett Colloidal Masks for Large Area Nanostructure Realization. *Thin Solid Films* **2020**, *709*, 138195.

[2] Tzadka, S.; Ureña Martin, C.; Toledo, E.; Yassin, A. A. K.; Pandey, A.; Le Saux, G.; Porgador, A.; Schvartzman, M. A Novel Approach for Colloidal Lithography: From Dry Particle Assembly to High-Throughput Nanofabrication. *ACS Appl. Mater. Interfaces* **2024**, *16* (14), 17846–17856, ref. (31) in main text.

[3] Pandey, A.; Nowakowski, P.; Ureña Martin, C.; Abu Ahmad, M.; Edri, A.; Toledo, E.; Tzadka, S.; Walther, J.; Le Saux, G.; Porgador, A.; Smith, A.-S.; Schvartzman, M. Membrane Fluctuation Model for Understanding the Effect of Receptor Nanoclustering on the Activation of Natural Killer Cells through Biomechanical Feedback. *Nano Lett.* **2024**, *24* (18), 5395−5402, ref. (28) in main text.

[4] Janeš, J. A.; Stumpf, H.; Schmidt, D.; Seifert, U.; Smith, A. S. Statistical Mechanics of an Elastically Pinned Membrane: Static Profile and Correlations. *Biophys. J.* **2019**, *116* (2), 283−295, ref. (43) in main text.

[5] Janeš, J. A.; Monzel, C.; Schmidt, D.; Merkel, R.; Seifert, U.; Sengupta, K.; Smith, A.-S. First-Principle Coarse-Graining Framework for Scale-Free Bell-Like Association and Dissociation Rates in Thermal and Active Systems. *Phys. Rev. X* **2022**, *12* (3), No. 031030, ref. (36) in main text.